Letter

Molecular beam epitaxy synthesis and electrical transport properties of the correlated kagome metal Ni_3In

Minyong Han,* Caolan John, Jingxu Zheng, Shiang Fang, and Joseph G. Checkelsky†
Department of Physics, Massachusetts Institute of Technology, Cambridge, Massachusetts 02139, USA

(Received 1 December 2023; revised 30 January 2024; accepted 4 March 2024; published 18 March 2024)

Ni_3In is a paramagnetic intermetallic consisting of *AB*-stacked Ni-kagome networks. Correlated electron behaviors deviating from the Fermi-liquid form have recently been observed in Ni_3In bulk single crystals, attributed to stabilization of a partially flat electronic band near the Fermi level. Synthesis of this system in thin-film form offers unique opportunities for tuning of materials that could aid in identifying the microscopic origin of the non-Fermi-liquid response and exploring the suspected quantum criticality therein. Here, we report the realization of (001)-oriented epitaxial thin films of Ni_3In on single-crystal $SrTiO_3$ (111) substrates by molecular beam epitaxy. Via control of growth conditions, we fabricate high-quality films with quantum fluctuations strongly influencing the physical properties of the system. Analysis of the electrical transport response reveals that intrinsic spin fluctuations in Ni_3In may account for the observed non-Fermi-liquid behavior. Such structures may facilitate driving Ni_3In across a potential quantum critical phase transition and uncover the role of unusual flat bands in triggering correlated phenomena.

DOI: 10.1103/PhysRevB.109.L121112

Introduction. The paramagnetic metal Ni_3In consists of *AB*-stacked two-dimensional Ni-kagome networks [Figs. 1(a) and 1(b)]. Compared to quasi-two-dimensional (quasi-2D) kagome metals in which such layers are interleaved with structurally distinct spacer layers [1–4], interkagome hybridization in T_3X (T = Mn, Fe, Ni; X = Ga, Ge, In, Sn) systems further facilitates a higher-dimensional electronic structure. As a consequence, T_3X have been reported to support distinct correlated and topological electronic behaviors [5–7], which are of considerable interest for understanding the variety of electronic phenomena possible in the kagome-metal family of materials.

Recent bulk single-crystal studies on Ni_3In have reported peculiar transport and thermodynamic responses deviated from the canonical Fermi-liquid expectations [8,9]. These non-Fermi-liquid (NFL) behaviors include T-linear resistivity persisting down to anomalously low temperature ($\sim$1 K) and deviation of the low-temperature heat capacity from the conventional T^3 dependence. Such behaviors were ascribed to the extremely flat band within the *ab* plane [Fig. 1(c), red-shaded area; referred to as a partial flat band] [8–11]. In addition, anomalous low-temperature Raman responses in this compound further revealed the relevance of this partial flat band in generating anisotropic Kondo lattice behaviors [9]. Given the breakdown of Fermi liquid in the system, the possibility of a quantum critical point in the proximate phase space has been raised [12–14].

A variety of kagome metals has been realized in epitaxial thin-film morphology [15–20]. In order to tune the NFL response in Ni_3In and explore the suspected quantum critical phase diagram, it is of significant interest to realize thin films of Ni_3In for the manipulation of material properties (via, e.g., epitaxial strain, quantum confinement, electrostatic gating). Here, we report the stabilization of high-quality Ni_3In thin films by molecular beam epitaxy. X-ray diffraction (XRD), transmission electron microscopy (TEM), and electron energy loss spectroscopy (EELS) altogether indicate the formation of single-crystalline Ni_3In with precise stoichiometry and conformal film morphology. Electrical transport reveals the NFL behaviors in good agreement with those observed in bulk single-crystal Ni_3In. A more detailed analysis of its magnetotransport properties suggests spin fluctuations at the origin of the Fermi-liquid breakdown.

Epitaxial thin-film synthesis and structural characterizations. Ni_3In thin films were grown on single -crystal $SrTiO_3$ (111) substrates (Shinkosha, Co.). Prior to film synthesis, the substrates were dipped into buffered oxide etch for 8 min and then rinsed with deionized water. This chemical etching procedure was followed by 1 h annealing in air at 1300 °C. Substrates prepared this way had flat and step-terraced surface morphologies. After loading into the molecular beam epitaxy (MBE) chamber, we pre-annealed the substrates at 60 °C for 1 h to eliminate heterogeneous adsorbates. Then, the substrate temperature was ramped down to the deposition temperature of $100 \leqslant T_d \leqslant 300$ °C at which Ni and In were co-deposited by thermal evaporation from solid source effusion cells. The ratio of beam-equivalent pressures (BEPs) was P_{Ni}:P_{In} = 1:1.8, where P_{Ni} and P_{In} are BEPs for Ni and In, respectively. The BEPs were calibrated before each growth to ensure a consistent deposition rate of $\sim$1 nm/min. The resultant film thickness (t_{film}) was confirmed by a quartz crystal monitor. After deposition, some of these films were postannealed to improve crystalline quality.

*Present address: Department of Applied Physics, Stanford University, Stanford, CA 94305, USA.
†Corresponding author: checkelsky@mit.edu

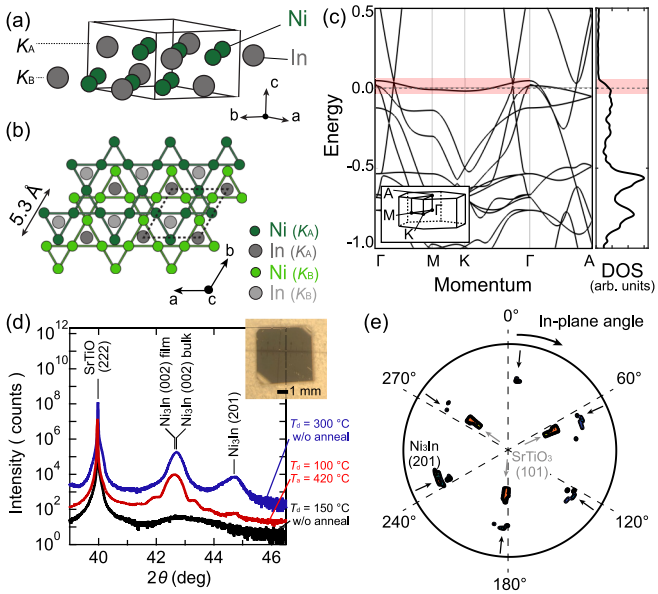

FIG. 1. (a) Schematic crystal structure and (b) the top view of the Ni_3In unit cell. (c) Electronic structure (left) and density of states spectrum (right). Inset: The Brillouin zone. The partial flat band is shaded in red. (d) X-ray diffraction spectra of Ni_3In films with (red) and without (black, blue) the postannealing treatments. Inset: Optical micrograph of a Ni_3In film (scale bar: 1 mm). (e) Pole figure of a Ni_3In film, displaying in-plane crystallographic orientation of the film with respect to the $SrTiO_3$ substrate. Intensities associated with the Ni_3In (201) diffraction peaks and the $SrTiO_3$ (101) diffraction peaks are marked with black and gray arrows, respectively. The radial axis denotes the inclination angle with respect to the film normal vector.

Figure 1(d) shows XRD spectra of $t_{\mathrm{film}} = 20$ nm samples with (red) and without (black, blue) postannealing treatments. The wavelength of the incident x-ray beam was $\lambda = 0.154$ nm. In the vicinity of the $SrTiO_3$ (222) XRD peak at $2\theta = 39.98°$, film XRD peaks were observed. The film deposited at $T_{\mathrm{d}} = 140\,°\mathrm{C}$ shows a broad and low-intensity peak around $2\theta = 42.70°$, the (002) XRD peak position for bulk Ni_3In [Fig. 1(d), black]. This indicates the formation of a c-axis-oriented Ni_3In film with low crystalline quality when T_{d} is below the In melting point $T_{\mathrm{m,In}} = 156.6\,°\mathrm{C}$. The film deposited at $T_{\mathrm{d}} = 300\,°\mathrm{C}$ shows a well-defined and high-intensity peak at $2\theta = 42.70°$, together with another satellite peak at $2\theta = 44.70°$ [Fig. 1(d), blue]. The position of the latter is the (201) XRD peak position for bulk Ni_3In, suggesting the formation of a high-crystalline, but less singly oriented Ni_3In film when $T_{\mathrm{d}} > T_{\mathrm{m,In}}$. This tendency suggests that the film-substrate epitaxial interaction becomes less relevant in the T_{d} regime where In atoms have large kinetic energy. In order to attain high-crystalline quality while maintaining single-crystallographic orientation, we deposited the films at $T_{\mathrm{d}} = 100\,°\mathrm{C}$ ($< T_{\mathrm{m,In}}$) and subsequently annealed them at $T_{\mathrm{a}} = 420\,°\mathrm{C}$ ($> T_{\mathrm{m,In}}$) for 1 h. The XRD spectrum of such a film shows a well-defined peak with pronounced intensity at $2\theta_{\mathrm{film,(002)}} = 42.65°$ (0.1% deviated from $2\theta_{\mathrm{bulk,(002)}}$) and suppressed intensity at $2\theta_{\mathrm{bulk,(201)}} = 44.70°$ [Fig. 1(d), red].

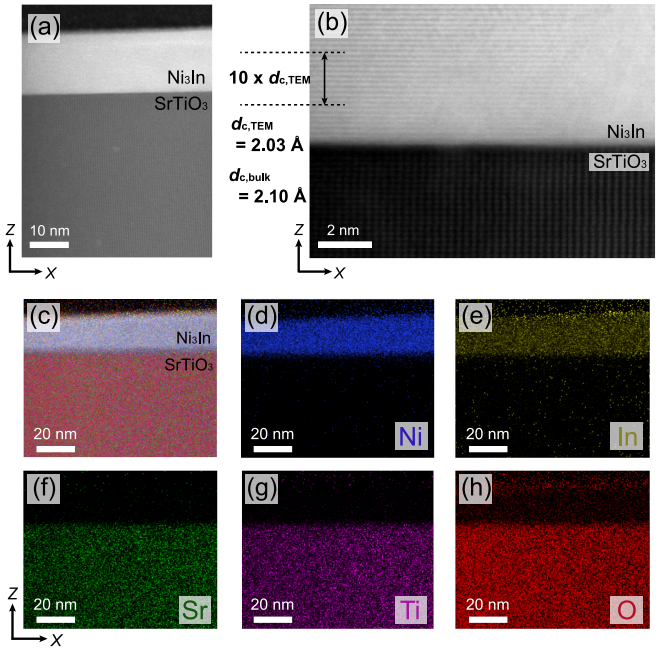

FIG. 2. Cross-section transmission electron microscopy images of a Ni_3In thin film with 16 nm thickness taken at (a) low magnification and (b) high magnification. (c) Electron energy loss spectroscopy measurement and (d)–(h) element-specific mappings for Ni, In, Sr, Ti, and O, respectively.

Laue interference fringes were observed on both sides of the film peak, indicating sharp interfaces.

The epitaxial relation between Ni_3In and $SrTiO_3$ was characterized by asymmetric XRD measurements. A collection of Ni_3In (201) diffraction peaks and $SrTiO_3$ (101) diffraction peaks is shown in the pole figure in Fig. 1(e). The Ni_3In (201) peaks [black arrows in Fig. 1(e)] manifest sixfold rotation symmetry as expected from the hexagonal crystal symmetry, whereas the $SrTiO_3$ (101) peaks [gray arrows in Fig. 1(e)] manifest threefold rotation symmetry as expected from the trigonal symmetry of the (111) facet of a cubic crystal. The in-plane angles of the Ni_3In (201) peaks are matched with those of the $SrTiO_3$ (101) peaks, indicating epitaxial alignment of in-plane crystallographic orientations between the two layers.

The structural analyses based on XRD were corroborated with other spectroscopic measurements. Figures 2(a) and 2(b) are cross-section TEM images of a $t_{\mathrm{film}} = 16$ nm sample. The low-magnification TEM image [Fig. 2(a)] reveals a conformally coated film morphology; the observed t_{film} is estimated to be 15.3 nm, ~4% deviated from the calibrated t_{film}. The higher-magnification TEM image [Fig. 2(b)] more clearly visualizes the atomic arrangements in both the Ni_3In film and $SrTiO_3$ substrate. In agreement with the x-ray measurements, the Ni_3In c axis is aligned with the film normal direction and the interkagome distance is found to be $d_{\mathrm{c,TEM}} = 2.03$ Å. This is close to the interkagome distance in bulk Ni_3In (i.e., $d_{\mathrm{c,bulk}} = 2.10$ Å).

Additionally, we conducted EELS for an element-specific chemical identification. Each element is color coded in Figs. 2(d) and 2(e), and Fig. 2(c) is their superposition. Across the sharp film-substrate interface, Ni and In are present only

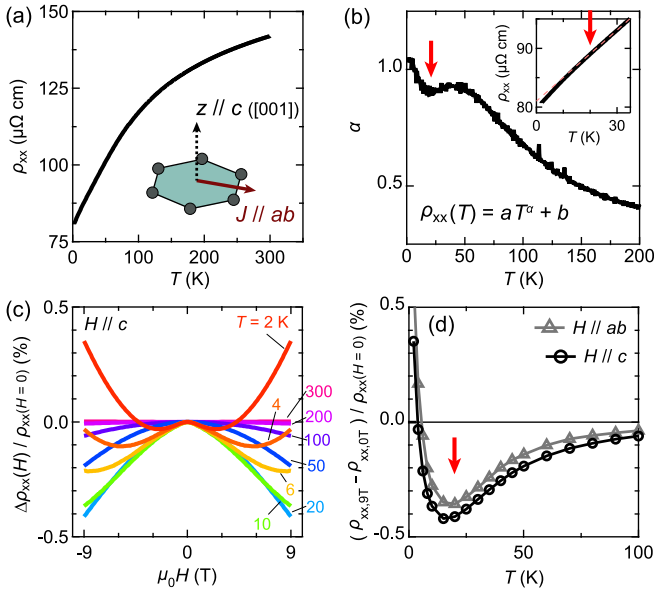

FIG. 3. (a) Temperature-dependent electrical resistivity $\rho_{xx}(T)$ of a Ni_3In thin film with 20 nm thickness. Inset: The relative orientation of the electrical current J with respect to the film normal vector z and the c axis of Ni_3In. (b) Temperature-dependent resistivity exponent α. Inset: Magnified view of (a) in the low-temperature regime (orange dashed line is a guide to the eye for the linear slope above 20 K). (c) Magnetoresistance (MR) at selected temperatures with magnetic field (H) along the c axis. (d) The $\mu_0 H = 9$ T MR at different temperatures with $H//c$ axis (black) and $H//ab$ plane (gray). Red arrows in (b) and (d) mark the features at $T = 20$ K.

in the top layer [Figs. 2(d) and 2(e)], whereas Sr, Ti, and O can be found only in the bottom layer [Figs. 2(f)–2(h)]; note that nearly overlapping core loss edges of Ti and In may produce a small In signal in $SrTiO_3$ even in the absence of a significant amount of In. As expected from the 3:1 stoichiometry, the intensity from Ni is stronger than that from In. At the top surface of the Ni_3In film, a finite intensity is observed from O, which we hypothesize to be a thin layer of surface oxidation from air exposure.

Electrical transport measurements. The electrical transport properties of Ni_3In films were characterized down to $T = 1.8$ K. Figure 3(a) shows the temperature-dependent electrical resistivity $\rho_{xx}(T)$ of a postannealed sample with $t_{\text{film}} = 20$ nm. The overall temperature dependence reveals a metallic character with decreasing ρ_{xx} as T decreases. The resistivity at $T = 300$ and 1.8 K is 142 and 80.6 μΩ cm, respectively, giving the residual resistivity ratio of RRR = 1.76. Films with $t_{\text{film}} = 90$ nm (10 nm) prepared by the equivalent growth conditions also showed a metallic character with $\rho_{xx} = 201$ μΩ cm (128 μΩ cm) and $\rho_{xx} = 38.5$ μΩ cm (94.9 μΩ cm) at 300 and 1.8 K, respectively, and RRR = 5.20 (1.35).

Within $100 \leqslant T \leqslant 300$ K, $\rho_{xx}(T)$ of the $t_{\text{film}} = 20$ nm sample shows a nonlinear temperature dependence with larger $d\rho_{xx}/dT$ at lower temperature (i.e., $d^2\rho_{xx}/dT^2 < 0$). This tendency can also be extracted from the resistivity exponent α, assuming $\rho_{xx} \propto T^{\alpha}$ [Fig. 3(b)]. α is inferred from the relation $\alpha = T(d\rho_{xx}/dT)/(\rho_{xx} - \rho_{xx,0})$, where $\rho_{xx,0}$ is the extrapolated ρ_{xx} value at $T = 0$ K. The sublinear exponent ($\alpha < 1$) at $T \geqslant 100$ K is consistent with $d^2\rho_{xx}/dT^2 < 0$ within this T range. Qualitatively similar nonlinearity was observed down to 100 K in all studied films with $10 \leqslant t_{\text{film}} \leqslant 90$ nm.

At $T < 100$ K, the T linearity of $\rho_{xx}(T)$ is approximately restored and persists down to $T = 1.8$ K. In a bulk report of Ni_3In, the T^2 rollover in $\rho_{xx}(T)$ was observed below ∼1 K; this is much lower than the typical temperature regime below which the T-linear electron-phonon scattering rate gives way to a T-quadratic electron-electron scattering rate within the Fermi-liquid paradigm [8]. With $\rho_{xx}(T)$ deviated significantly from the canonical Fermi-liquid expectation, we identify this $1 < T \ll 100$ K regime to stabilize a NFL state in Ni_3In. A closer inspection of the NFL state reveals another inflection-like feature in $\rho_{xx}(T)$. As T drops below 20 K, $d\rho_{xx}/dT$ increases additionally by a small amount [Fig. 3(b), inset]. This behavior is also manifested as a small dip in α within a narrow T range near 20 K; $\alpha < 1$ within the dip and $\alpha \sim 1$ above and below that, reflecting two distinct linear slopes with respect to 20 K. As will be described further below, the feature at 20 K reflects a crucial energy scale of the NFL state that is suggestive of the nature of the underlying quantum fluctuations.

All samples within the $10 \leqslant t_{\text{film}} \leqslant 90$ nm thickness range, regardless of respective electronic quality and absolute values of resistivity, showed qualitatively similar features in $\rho_{xx}(T)$ at the same temperatures as in the $t_{\text{film}} = 20$ nm sample, including the nonlinearity down to $T = 100$ K and the small change in $d\rho_{xx}/dT$ (or sublinear dip in α) around $T = 20$ K. The Mott-Ioffe-Regel limit of resistivity in this system is estimated to be $\rho_{\text{MIR}} = (3\pi^2\hbar)/(e^2 k_F^2 l_{\text{MFP}}) = 2.3$ mΩ cm using the mean free path l_{MFP} equal to the in-plane lattice constant $d_{ab} = 5.3$ Å and the Fermi wave vector $k_F \sim 0.45$/Å of the nearly isotropic hole pocket at the Γ point [8,21]; an experimentally measurable Mott-Ioffe-Regel limit is expected to be the mean value of ρ_{MIR} for multiple bands in the system and contributions from other bands with smaller k_F are expected to shift it further towards higher resistivity. In all measured samples, the resistivity at $1.8 \leqslant T \leqslant 300$ K was consistently within $38.5 \leqslant \rho_{xx} \leqslant 201$ μΩ cm, significantly smaller than the estimated ρ_{MIR}. This suggests that the observed anomalies in electrical transport arise from the intrinsic scattering properties of Ni_3In, rather than disorder-induced saturation of scattering rates as is frequently observed in bad metals.

Figure 3(c) shows the magnetoresistance (MR $\equiv [\rho_{xx}(H) - \rho_{xx}(H=0)]/\rho_{xx}(H=0)$) of this sample within $2 \leqslant T \leqslant 300$ K, where H is the magnetic field. H was applied along the c axis of Ni_3In. At $T = 300$ K, we see a small positive MR with 0.002% amplitude at $\mu_0 H = 9$ T, likely originating from the Lorentz-force deflection of electrons. As T decreases, it gives way to a small negative MR with −0.002% amplitude at $\mu_0 H = 9$ T at $T = 250$ K. In a bulk study of Ni_3In, the onset of negative MR at $T < 300$ K was ascribed to the formation of localized magnetic moments and subsequent field suppression of the associated magnetic fluctuations [8]. This may also account for the nonlinear $\rho_{xx}(T)$ in the $100 \leqslant T \leqslant 300$ K regime, within which the local moments become increasingly well defined at lower T and generate a nonmonotonic temperature dependence of

scattering cross sections for conduction electrons. We note that a similar tendency has been identified in a wide class of nearly magnetic systems, in which strong fluctuation between spinful and spinless states generates a saturating $\rho_{xx}(T)$ at high temperature [22].

The quadratic negative MR enhances as T decreases, reaching up to -0.42% at $\mu_0 H = 9$ T at $T = 20$ K. At $T <$ 20 K, however, the MR begins to manifest a nonquadratic field dependence. We hypothesize that this nonquadraticity originates from the superposition of the positive MR component (increasing due to higher electronic mobility at lower T) and the negative MR component (increasing due to higher moment size at lower T). As a result of the two competing contributions, the net MR response below 20 K changes from negative (i.e., $d\rho_{xx}/dH < 0$) in the low-field regime to positive (i.e., $d\rho_{xx}/dH > 0$) in the high-field regime. The positive MR component tends to dominate at lower T and the 9 T MR at 2 K becomes positive with 0.35% amplitude.

Figure 3(d) summarizes the 9 T MR amplitudes at different T for $H//c$ (black) and $H//ab$ (gray). Qualitatively similar trends are observed for both field orientations. In bulk single-crystal Ni_3In, χ_c and χ_{ab} showed a Curie-Weiss-type temperature dependence with $\chi_c > \chi_{ab}$ within $2 \leqslant T \leqslant 300$ K, where χ_c and χ_{ab} denote magnetic susceptibility under $H//c$ and $H//ab$, respectively [8]. The former observation is consistent with the presence of local magnetic moments in Ni_3In and the latter suggests more effective field suppression of magnetic fluctuations when $H//c$, consistent with our observation that the negative MR component is larger for $H//c$ ([Fig. 3(d)].

The gradual crossover from the net negative MR ($T >$ 20 K) to the net positive MR ($T < 20$ K) can be understood as an emergence of spin-spin coherence in Ni_3In—a possibility also raised in bulk studies of Ni_3In [8,9]. To examine this hypothesis, we scaled the MR response with respect to $\mu_0 H/(T + T_{coh})$, akin to the incoherent spin-fluctuation model frequently applied in analyzing the MR responses of heavy fermion systems, where T_{coh} is the temperature above/below which spins are incoherent/coherent [23–26]. Recently, the scope of this model has been expanded to describe, in general, the effects of local moments on MR responses in metallic systems, not restricted to those from the f electrons [27–29]. Here, we assume $T_{coh} = 20$ K given the inflectionlike feature in $\rho_{xx}(T)$ at $T = 20$ K; unlike in dilute Kondo systems where a sharp drop in ρ_{xx} is expected at T_{coh}, spin-spin coherence formation in multiband metals is known to manifest as a small slope change in $\rho_{xx}(T)$ [27]. Within $20 \leqslant T \leqslant 250$ K, the MR traces at different T plotted against the $\mu_0 H/(T + T_{coh})$ scale reasonably well [Fig. 4(a)]. This scaling analysis at $T > T_{coh}$ suggests that the system in the zero-field state in fact contains an ensemble of incoherently fluctuating spins. We note that reasonable scaling fits could be obtained with $T_{coh} \sim (20 \pm 5)$ K for all studied samples at $T > T_{coh}$ (the error bar originating from the uncertainty in the goodness of fit), potentially correlated with the consistent occurrence of the inflectionlike feature in $\rho_{xx}(T)$ at $T = 20$ K for all t_{film}. In contrast, the MR traces below 20 K deviate significantly from the scaling curves above 20 K [Fig. 4(b)]. The failure of this scaling analysis at $T < T_{coh}$ suggests the insufficiency of the incoherent spin-fluctuation model in fully accounting for the MR response in this T regime. As

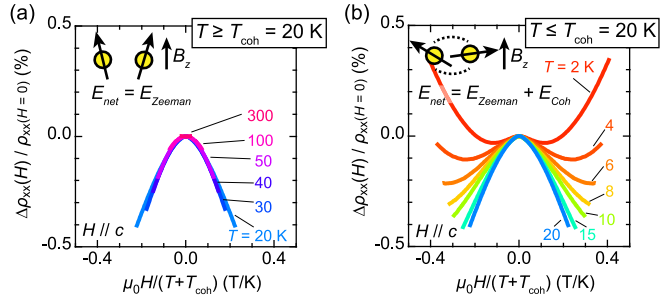

FIG. 4. Temperature-field scaling analysis of the magnetoresistance (MR) response based on the incoherent spin fluctuation model. The MR traces in Fig. 3(c) are plotted against $\mu_0 H/(T + T_{coh})$ for (a) $T \geqslant 20$ K and (b) $T \leqslant 20$ K, with $T_{coh} = 20$ K.

depicted in the schematic inset in Fig. 4(b), we hypothesize that the spin-spin coherence energy (E_{coh}) counteracts the field polarization of individual spins (driven by the Zeeman energy E_{Zeeman}), leading to the suppression of the negative MR component and enabling the positive MR component to dominate the net response. A recent Raman scattering study on bulk Ni_3In has also captured a consistent incoherent-coherent crossover with strong polarization dependence, based on which the formation of the anisotropic Kondo lattice involving the partial flat band was discussed [9]. Regarding estimation of T_{coh}, the MR traces started to deviate from the scaling curve above T_{coh} when $T_{coh} \leqslant 15$ K was used, whereas reasonable scaling behavior persisted even below T_{coh} for $T_{coh} \geqslant 25$ K; this suggests $T_{coh} \sim 20$ K (see the Supplemental Material [30]). Overall, this framework suggests that complex actions of fluctuating local moments potentially associated with the partial flat band may account for the quantum fluctuations and its derived NFL state in Ni_3In.

Conclusion. In conclusion, we report the synthesis and characterization of correlated kagome metal Ni_3In in epitaxial thin-film form. Precise synthesis control and appropriate postannealing treatment in molecular beam epitaxy facilitate the stabilization of high-quality Ni_3In film with NFL responses, in agreement with previous bulk single-crystal studies [8,9]. The values of electrical resistivity in all the studied samples are significantly smaller than the Mott-Ioffe-Regel limit of resistivity, suggesting that the observed anomalies arise from the intrinsic quantum fluctuations in Ni_3In rather than disorder-dominated scatterings in the bad metal regime. A close inspection of its electrical transport properties reveals that fluctuating spins and their coherence formation may be responsible for the observed NFL behaviors. Previous studies of bulk Ni_3In have proposed possible connections between the partial flat band, local moments, and various anisotropic physical properties [8,9]. It is of significant interest to further investigate the nature of the fluctuating local moments and partial flat band. The high-quality Ni_3In films will offer a promising platform to engineer the NFL response and other flat-band-driven effects via epitaxial strain [31], quantum confinement [32], and electrostatic gating [33].

Acknowledgments. We are grateful to L. Ye, P. M. Neves, and R. McTigue for fruitful discussions. This work was funded, in part, by the Gordon and Betty Moore Foundation EPiQS Initiative, Grant No. GBMF9070 (J.G.C.) (synthesis

instrumentation), ARO Grant No. W911NF-16-1-0034 (characterization instrumentation), the Center for Advancement of Topological Semimetals, an Energy Frontier Research Center funded by the U.S. Department of Energy Office of Science, Office of Basic Energy Sciences, through the Ames Laboratory under Contract No. DE-AC02-07CH11358 (material development), and NSF Grant No. DMR-2104964 (electrical characterization). C.J. acknowledges support from STC Center for Integrated Quantum Materials, NSF Grant No. DMR-1231319.

[1] L. Ye, M. Kang, J. Liu, F. von Cube, C. R. Wicker, T. Suzuki, C. Jozwiak, A. Bostwick, E. Rotenberg, D. C. Bell, L. Fu, R. Comin, and J. G. Checkelsky, Massive Dirac fermions in a ferromagnetic kagome metal, Nature (London) **555**, 638 (2018).

[2] L. Ye, M. K. Chan, R. D. McDonald, D. Graf, M. Kang, J. Liu, T. Suzuki, R. Comin, L. Fu, and J. G. Checkelsky, de Haas–van Alphen effect of correlated Dirac states in kagome metal Fe_3Sn_2, Nat. Commun. **10**, 4870 (2019).

[3] M. Kang, L. Ye, S. Fang, J.-S. You, A. Levitan, M. Han, J. I. Facio, C. Jozwiak, A. Bostwick, E. Rotenberg, M. K. Chan, R. D. McDonald, D. Graf, K. Kaznatcheev, E. Vescovo, D. C. Bell, E. Kaxiras, J. van den Brink, M. Richter, M. P. Ghimire *et al.*, Dirac fermions and flat bands in the ideal kagome metal FeSn, Nat. Mater. **19**, 163 (2020).

[4] M. Kang, S. Fang, L. Ye, H. C. Po, J. Denlinger, C. Jozwiak, A. Bostwick, E. Rotenberg, E. Kaxiras, J. G. Checkelsky, and R. Comin, Topological flat bands in frustrated kagome lattice CoSn, Nat. Commun. **11**, 4004 (2020).

[5] A. K. Nayak, J. E. Fischer, Y. Sun, B. Yan, J. Karel, A. C. Komarek, C. Shekhar, N. Kumar, W. Schnelle, J. Kübler, C. Felser, and S. S. P. Parkin, Large anomalous Hall effect driven by a nonvanishing Berry curvature in the noncollinear antiferromagnet Mn_3Ge, Sci. Adv. **2**, e1501870 (2016).

[6] K. Kuroda, T. Tomita, M.-T. Suzuki, C. Bareille, A. A. Nugroho, P. Goswami, M. Ochi, M. Ikhlas, M. Nakayama, S. Akebi, R. Noguchi, R. Ishii, N. Inami, K. Ono, H. Kumigashira, A. Varykhalov, T. Muro, T. Koretsune, R. Arita, S. Shin *et al.*, Evidence for magnetic Weyl fermions in a correlated metal, Nat. Mater. **16**, 1090 (2017).

[7] A. A. Burkov and L. Balents, Weyl semimetal in a topological insulator multilayer, Phys. Rev. Lett. **107**, 127205 (2011).

[8] L. Ye, S. Fang, M. Kang, J. Kaufmann, Y. Lee, C. John, P. M. Neves, S. Y. F. Zhao, J. Denlinger, C. Jozwiak, A. Bostwick, E. Rotenberg, E. Kaxiras, D. C. Bell, O. Janson, R. Comin, and J. G. Checkelsky, Hopping frustration-induced flat band and strange metallicity in a kagome metal, Nat. Phys. (2024)

[9] D.-H. Gim, D. Wulferding, C. Lee, H. Cui, K. Nam, M. J. Han, and K. H. Kim, Fingerprints for anisotropic Kondo lattice behavior in the quasiparticle dynamics of the kagome metal Ni_3In, Phys. Rev. B **108**, 115143 (2023).

[10] S. V. Vonsovskii, M. I. Katsnel'son, and A. V. Trefilov, Localized and itinerant behavior of electrons in metals, Phys. Met. Metallogr. **76**, 247 (1993).

[11] N. Regnault, Y. Xu, M.-R. Li, D.-S. Ma, M. Jovanovic, A. Yazdani, S. S. P. Parkin, C. Felser, L. M. Schoop, N. P. Ong, R. J. Cava, L. Elcoro, Z.-D. Song, and B. A. Bernevig, Catalogue of flat-band stoichiometric materials, Nature (London) **603**, 824 (2022).

[12] G. R. Stewart, Non-Fermi-liquid behaviors in d- and f-electron metals, Rev. Mod. Phys. **73**, 797 (2001).

[13] P. Coleman and A. J. Schofield, Quantum criticality, Nature (London) **433**, 226 (2005).

[14] H. v. Löhneysen, A. Rosch, M. Vojta, and P. Wölfle, Fermi-liquid instabilities at magnetic quantum phase transitions, Rev. Mod. Phys. **79**, 1015 (2007).

[15] H. Inoue, M. Han, L. Ye, T. Suzuki, and J. G. Checkelsky, Molecular beam epitaxy growth of antiferromagnetic kagome metal FeSn, Appl. Phys. Lett. **115**, 072403 (2019).

[16] M. Han, H. Inoue, S. Fang, C. John, L. Ye, M. K. Chan, D. Graf, T. Suzuki, M. P. Ghimire, W. J. Cho, E. Kaxiras, and J. G. Checkelsky, Evidence of two-dimensional flat band at the surface of antiferromagnetic kagome metal FeSn, Nat. Commun. **12**, 5345 (2021).

[17] D. Hong, C. Liu, H.-W. Hsiao, D. Jin, J. E. Pearson, J.-M. Zuo, and A. Bhattacharya, Molecular beam epitaxy of the magnetic Kagome metal FeSn on $LaAlO_3$ (111), AIP Adv. **10**, 105017 (2020).

[18] D. Khadka, T. R. Thapaliya, S. Hurtado Parra, J. Wen, R. Need, J. M. Kikkawa, and S. X. Huang, Anomalous Hall and Nernst effects in epitaxial films of topological kagome magnet Fe_3Sn_2, Phys. Rev. Mater. **4**, 084203 (2020).

[19] A. Markou, J. M. Taylor, A. Kalache, P. Werner, S. S. P. Parkin, and C. Felser, Noncollinear antiferromagnetic Mn_3Sn films, Phys. Rev. Mater. **2**, 051001(R) (2018).

[20] K. Fujiwara, J. Ikeda, J. Shiogai, T. Seki, K. Takanashi, and A. Tsukazaki, Ferromagnetic $Co_3Sn_2S_2$ thin films fabricated by co-sputtering, Jpn. J. Appl. Phys. **58**, 050912 (2019).

[21] O. Gunnarsson, M. Calandra, and J. E. Han, Colloquium: Saturation of electrical resistivity, Rev. Mod. Phys. **75**, 1085 (2003).

[22] R. Jullien, M. T. Béal-Monod, and B. Coqblin, Resistivity of nearly magnetic metals at high temperatures: Application to neptunium and plutonium, Phys. Rev. B **9**, 1441 (1974).

[23] T. A. Costi, Kondo effect in a magnetic field and the magnetoresistivity of Kondo alloys, Phys. Rev. Lett. **85**, 1504 (2000).

[24] D. Kaczorowski, B. Andraka, R. Pietri, T. Cichorek, and V. I. Zaremba, Heavy-fermion behavior in YbPtIn, Phys. Rev. B **61**, 15255 (2000).

[25] A. Malinowski, M. F. Hundley, C. Capan, F. Ronning, R. Movshovich, N. O. Moreno, J. L. Sarrao, and J. D. Thompson, c-axis magnetotransport in $CeCoIn_5$, Phys. Rev. B **72**, 184506 (2005).

[26] B. Batlogg, D. J. Bishop, E. Bucher, B. Golding Jr., A. P. Ramirez, Z. Fisk, J. L. Smith, and H. R. Ott, Superconductivity and heavy fermions, J. Magn. Magn. Mater. **63-64**, 441 (1987).

[27] C. Liu, V. F. C. Humbert, T. M. Bretz-Sullivan, G. Wang, D. Hong, F. Wrobel, J. Zhang, J. D. Hoffman, J. E. Pearson, J. S. Jiang, C. Chang, A. Suslov, N. Mason, M. R. Norman, and A. Bhattacharya, Observation of an antiferromagnetic quantum critical point in high-purity $LaNiO_3$, Nat. Commun. **11**, 1402 (2020).

[28] A. Patra, K. P. Maity, and V. Prasad, Influence of orbital two-channel Kondo effect on anomalous Hall effect in ferrimagnetic composites of ferrimagnetic composites of $LaNiO_3$ and $CoFe_2O_4$, J. Phys.: Condens. Matter **31**, 255702 (2019).

[29] R. P. Khosla and J. R. Fischer, Magnetoresistance in degenerate CdS: Localized magnetic moments, Phys. Rev. B **2**, 4084 (1970).

[30] See Supplemental Material at http://link.aps.org/supplemental/10.1103/PhysRevB.109.L121112 for magnetoresistance scaling analyses with different values of T_{coh}.

[31] B. Burganov, C. Adamo, A. Mulder, M. Uchida, P. D. C. King, J. W. Harter, D. E. Shai, A. S. Gibbs, A. P. Mackenzie, R. Uecker, M. Bruetzam, M. R. Beasley, C. J. Fennie, D. G. Schlom, and K. M. Shen, Strain control of fermiology and many-body interactions in two-dimensional ruthenates, Phys. Rev. Lett. **116**, 197003 (2016).

[32] H. Inoue, M. Han, M. Hu, T. Suzuki, J. Liu, and J. G. Checkelsky, Band engineering of a magnetic thin film rare-earth monopnictide: A platform for high Chern number, Phys. Rev. Mater. **3**, 101202(R) (2019).

[33] A. Kumar, N. C. Hu, A. H. MacDonald, and A. C. Potter, Gate-tunable heavy fermion quantum criticality in a moiré Kondo lattice, Phys. Rev. B **106**, L041116 (2022).